*Article*

# BiVO$_4$-Based Systems Magnetron Sputtered with Silver Nanoparticles for the Artificial Photosynthesis Reaction

Eva Naughton [1], Emerson C. Kohlrausch [2], Jesum Alves Fernandes [2] and James A. Sullivan [1,*]

[1] School of Chemistry, University College Dublin, Belfield, D18 V1W8 Dublin, Ireland; eva.naughton@ucd.ie
[2] School of Chemistry, University of Nottingham, University Park, Nottingham NG7 2RD, UK; emerson.kohlrausch@nottingham.ac.uk (E.C.K.); jesum.alvesfernandes@nottingham.ac.uk (J.A.F.)
[*] Correspondence: james.sullivan@ucd.ie

**Abstract:** The incorporation of Ag nanoparticles onto BiVO$_4$ (a known H$_2$O oxidising photocatalyst) through magnetron sputtering to form a composite was studied. ICP-OES results showed that the loading of Ag on BiVO$_4$ was below 1% in all cases. UV-Vis DRS and CO$_2$-TPD analyses demonstrated that upon incorporation of Ag onto BiVO$_4$, an increase in the extent of visible light absorption and CO$_2$ adsorption was seen. TEM imaging showed the presence of Ag particles on the surface of larger BiVO$_4$ particles, while XRD analysis provided evidence for some doping of Ag into BiVO$_4$ lattices. The effect of the composite formation on the activity of the materials in the artificial photosynthesis reaction was significant. BiVO$_4$ alone produces negligible amounts of gaseous products. However, the Ag-sputtered composites produce both CO and CH$_4$, with a higher loading of Ag leading to higher levels of product formation. This reactivity is ascribed to the generation of a heterojunction in the composite material. It is suggested that the generation of holes in BiVO$_4$ following photon absorption is used to provide protons (from H$_2$O oxidation), and the decay of an SPR response on the Ag NPs provides hot electrons, which together with the protons reduce CO$_2$ to produce CH$_4$, CO, and adsorbed hydrocarbonaceous species.

**Keywords:** magnetron sputtering; artificial photosynthesis; CO$_2$ photoreduction; BiVO$_4$ photocatalysts

## 1. Introduction

Currently, about 80% of global energy is generated through the combustion of fossil fuels such as coal, oil, and natural gas [1]. With projected population growth, energy demand is expected to rise further [2]. However, this continued reliance on fossil fuels will not only lead to their eventual depletion but also cause significant environmental harm, including localised air pollution, and the intensification of the greenhouse effect, contributing to global warming [3].

While CO$_2$ (a greenhouse gas (GHG)) is naturally generated from fossilised materials at a very slow rate, human activities (e.g., fossil fuel combustion and land-use changes) have disrupted the carbon cycle, resulting in an excess accumulation of CO$_2$ in the atmosphere [4].

One promising long-term strategy to reduce atmospheric CO$_2$ emissions is carbon capture and utilisation (CCU), which involves capturing CO$_2$ after its formation and using it to produce valuable chemicals, materials, or fuels [5]. However, because CO$_2$ has strong carbon–oxygen (C=O) bonds, converting it into most other compounds is an endothermic process, requiring the input of energy [6].

Photocatalysis, which uses light to drive chemical reactions in the presence of a catalyst, has gained significant attention in recent years, particularly in environmental and sustainable chemistry applications like artificial photosynthesis (AP). The reaction of $CO_2$ with water to produce carbon monoxide (CO) or hydrocarbons using a sustainable energy source is particularly appealing, as it could reduce atmospheric $CO_2$ levels while generating renewable fuels or chemical precursors. Success in this area would also support the broader goal of establishing a circular carbon economy.

In this context, the use of semiconductor materials has attracted significant research interest, particularly in the field of photocatalysis and its application to AP [7–12].

To perform AP using a semiconductor photocatalyst, the catalyst must meet two key energetic criteria. First, the conduction band (CB) minimum must be at a higher energy level (more negative potential) than the energy required for $CO_2$ reduction. Second, the valence band (VB) maximum must be at a lower energy level than the potential needed for oxygen ($O_2$) evolution. As illustrated in Figure 1, while some semiconductors, such as $TiO_2$ and TaNO, possess suitable band energies for catalysing AP, others do not. For example, $BiVO_4$ lacks a CB minimum with sufficient energy to reduce $CO_2$, and Si's VB maximum is not low enough to effectively oxidise water ($H_2O$). To overcome these limitations and enable AP, such materials may be paired with a 'co-catalyst' [13–15].
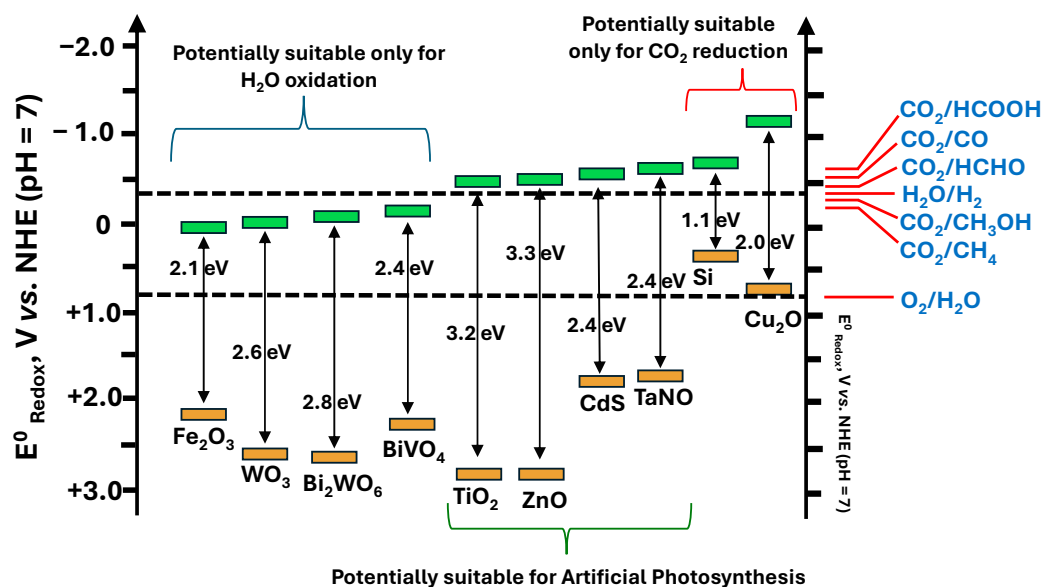


**Figure 1.** Valence (VB) and conduction (CB) band-edge positions of some semiconductors relative to the energy levels of the redox couples involved in the reduction of $CO_2$ and oxidation of $H_2O$ vs. NHE at pH = 7. Values for $CB_m$ and $VB_m$ obtained from Tamirat et al. [16].

$BiVO_4$ is a promising semiconductor for photochemical water splitting as it is stable, low cost, non-toxic, and has a moderate band gap ($E_g$) allowing it to absorb visible light [17]. The $E_g$ of $BiVO_4$ is approximately 2.46 eV (which equates to a visible light wavelength of 504 nm), with a valence band maximum of 2.86 V, and a conduction band minimum of 0.4 V vs. NHE at pH = 0 [18]. This means it has the potential to split water and act as an oxidation photocatalyst as the VB maximum lies below the oxidation potential of water. However, it cannot reduce $CO_2$ as its CB energy is not sufficiently high.

In an attempt to overcome this limitation, in this work, $BiVO_4$ was magnetron sputtered with Ag nanoparticles. The addition of noble metals to semiconductors is a well-studied method of increasing photocatalytic efficiency. Among the noble metals, silver is a popular choice due to its high photo-absorption and electrical conductivity, as well as the fact it is non-toxic [19]. $Ag/BiVO_4$ composites have proven active in many different

types of photocatalytic reactions. For example, Ag-doped $BiVO_4$ thin films prepared by magnetron sputtering were 2.3 times more active in the photodegradation of Rhodamine B than pristine $BiVO_4$ [20]. Hydrothermal synthesis of Ag-doped $BiVO_4$ microspheres yielded a material that could photodegrade 76% of methylene blue in a solution in 6 h, compared to a photodegradation efficiency of approximately 40% over pure $BiVO_4$ [21]. A $BiVO_4$ material coated with 7 wt% graphene and 0.003 wt% particulate Ag exhibited photocatalytic activity more than five times that of a $BiVO_4$ analogue in an AP reaction under flow conditions [22]. These increases in activity are attributed to the lower rates of electron/hole recombination in the Ag-containing systems due to the heterojunctions formed at the Ag-$BiVO_4$ interfaces which lead to more effective charge carrier separation, the generation of plasmonic electrons that can be catalytically useful following absorption of visible light, and variations in the band structure of $BiVO_4$ which may allow the material to both oxidise water and reduce $CO_2$ [20–23].

Plasmonic nanostructures can function as co-catalysts alongside different semiconductors. According to Zhang et al., plasmonic nanoparticles enhance the transfer of excited electrons to acceptor molecules and reduce the recombination of photogenerated charges, leading to improved photocatalytic efficiency [24]. For example, the photocatalytic reduction of Cr(VI) by $BiVO_4$ was greatly enhanced by the addition of Ag due to both the enhanced visible light absorption from the surface plasmonic resonance of Ag and the increased lifetime of the charge carriers. Photocatalytic electrons can easily transfer from $BiVO_4$ to Ag at the metal–semiconductor interfaces, suppressing the recombination of electrons and holes [25]. Similar results have been seen when Ag was added to $BiVO_4$ for the photocatalytic degradation of 2,4-dichlorophenoxyacetic acid [26], and when Ag was added to g-$C_3N_4$ for photocatalytic $H_2$ evolution [27]. Previously in our lab, the addition of plasmonic $RuO_2$ was shown to increase the reactivity of various semiconductors when acting as a co-catalyst in the AP reaction [28,29].

Sputter deposition is a widely used technique employed to deposit thin films on substrates. Sputtering is a technique where ion bombardment of a source material (the target, Ag in this case) results in the ejection of surface atoms which are then deposited onto a second material (the substrate, $BiVO_4$ in this case). Magnetron sputtering uses plasma to complete ion bombardment. The term "magnetron" arises due to the use of magnets to confine the plasma's electrons near the surface of the target. This leads to a high density of the plasma which increases the deposition rate but also prevents damage to the substrate from ion bombardment. The advantages of using magnetron sputtering to deposit metals onto substrates over other techniques is that we can easily get uniformity, it is fast, cheap, needs only low temperatures for operation, and a high purity can be obtained.

While Ag/$BiVO_4$ and similar composites are widely reported in the literature for various reactions, including AP, to the best of our knowledge, no studies have explored the preparation of Ag/$BiVO_4$ composites via magnetron sputtering for the AP reaction. Existing research on Ag/$BiVO_4$ materials prepared by magnetron sputtering primarily focuses on their use in the photodegradation of organic dyes [20,23]. In contrast, for AP or related photocatalytic reactions, other synthesis methods such as hydrothermal [30,31], photodeposition [22], and electrodeposition [32] are typically employed.

This research looks at Ag/$BiVO_4$ materials prepared by magnetron sputtering of $BiVO_4$ with Ag to hold two different loadings of Ag particles. The loading of Ag NPs was changed by varying the sputtering current and these materials were characterised and then tested in the AP reaction to see if the above-mentioned reaction-enhancing mechanisms occur, leading to higher $CO_2$ conversions and photocatalytic efficiencies.

## 2. Materials and Methods

### 2.1. Materials

Bismuth nitrate pentahydrate[a] ($Bi(NO_3)_3 \cdot 5H_2O$) (99% pure), ammonium metavanadate[a] ($NH_4VO_3$) (99% pure), ethylenediaminetetraacetic acid[b] ($[CH_2N(CH_2CO_2H)_2]_2$) (99% pure), sodium hydroxide[c] (NaOH) (99% pure), and nitric acid[c] ($HNO_3$) (69%) were purchased from Fluka[a] (Fluka Chemicals Ltd, Gillingham, Dorset SP84JL, UK), Sigma-Aldrich[b] (Vale Road, Arklow, Co. Wicklow, Y14 EK18, Ireland), and Riedel de Haën[c] (Wunstorfer Str. 40, 30926 Seelze, Germany) and used without further purification. Deionised water was used throughout. (The superscript letters (a, b, c) indicate the supplier for each chemical: (a) Fluka, (b) Sigma-Aldrich, and (c) Riedel-de Haën).

### 2.2. Methods

#### 2.2.1. Synthesis of Photocatalysts

$BiVO_4$ was synthesised according to the preparation methods reported by Bai et al. [33] and Min et al. [17]. $BiVO_4$ was firstly synthesised by a facile hydrothermal method. $Bi(NO_3)_3 \cdot 5H_2O$ (2.42 g, $4.99 \times 10^{-3}$ moles) was added to 2M nitric acid (2 mL, $4 \times 10^{-3}$ moles) under constant stirring (denoted as solution A). Then, $NH_4VO_3$ (0.58 g, $4.96 \times 10^{-3}$ moles) was dissolved in a solution of 4M NaOH (10 mL, 0.04 moles) and EDTA (1 g, $3.42 \times 10^{-3}$ moles), which was denoted as solution B. EDTA can complex with metal cations in solution to form stable water-soluble complexes. Then, solution B was added dropwise to solution A under vigorous stirring, and the pH of the solution was adjusted to pH 7 using a $HNO_3$ solution (2M). Finally, the obtained mixed solution was sealed in a Teflon-lined stainless steel autoclave and heated for 10 h at 180 °C. The resulting solid was collected by filtration and washed with water.

Silver was then deposited onto the surface of the $BiVO_4$ catalyst using magnetron sputtering. The instrument used in this work was an ATC-Orion 5 UHV with load-lock by AJA International, Inc. Approximately 2.0 g of catalyst was placed in a glove box connected to the load-lock prior to deposition. The catalyst was then placed in the sample holder and loaded into the load-lock (which has a pressure of approximately $6 \times 10^{-6}$ torr). The sample was held there for 20 min before being transferred to the main chamber for sputter deposition. This process was to ensure that any adsorbed species on the substrate surface were desorbed. In the chamber, the sample holder was rotated in order to get a uniform coating of the target on the powder substrate. DC sputtering was used. The working distance between the target and the substrate was 120 mm. The power used was 33 W, the potential was 333 V, the flow of Ar was 20 mL/min, and the deposition time was 30 min for each sample. To get a higher loading of Ag on the samples, the current was altered. The different currents used were 100 and 250 mA. The formed composite samples were labelled $Ag/BiVO_4$ 100 and $Ag/BiVO_4$ 250.

The catalyst characterisation methods and parameters can be found in the Supplementary Materials.

#### 2.2.2. Photocatalytic Reactions

The catalytic performances of the materials were analysed under batch-reaction conditions using simulated solar light as the energy input (using an Atlas Suntest CPS+ solar simulator unit equipped with a Xe arc lamp with UV filters). The experiments were carried out with the reactant species ($CO_2$ and $H_2O$) in the gas phase. All the gas flows to the reactor were controlled and adjusted using previously calibrated mass flow controllers.

Approximately 20 mg of catalyst were loaded into a Pyrex reactor, and the reactor was placed in a furnace in the dark. The temperature was increased to 110 °C for 30 min under

a flow of argon (100 mL/min) to ensure surface cleanliness. The temperature was then lowered to 50 °C, and the rate of Ar flow was lowered to 45 mL/min.

A gas mixture of water vapour and argon was produced by flowing pure Ar (at a rate of 50 mL/min) through a gas bubbler vessel containing water at 60 °C. This mixture of Ar and $H_2O_{(g)}$ was then combined with a $CO_2$ flow (5 mL/min), and the total mixture passed over the material for 1 h. The composition of the gas mixture was as follows: Ar (91.4% *v/v*), $CO_2$ (5% *v/v*), and $H_2O$ (3.6% *v/v*). The system was then allowed to cool to 25 °C, the taps closed to isolate the reactant gases, and the reactor placed in the solar simulator. Gas aliquots were extracted periodically using a 500 µL Swagelok™ gastight syringe. A Varian 450-GC equipped with TCD and FID detectors was used to identify and quantify the gaseous products evolved during the photocatalytic tests.

## 3. Results and Discussion

### 3.1. Characterisation

Inductively coupled plasma combined with optical emission spectroscopy (ICP-OES) was used to determine the loading of Ag NPs deposited onto the semiconductor materials following the sputtering process. The results of this analysis are displayed in Table 1.

**Table 1.** Wt % loadings of Ag determined from ICP analysis.

| Sample | Wt. % Ag | Colour |
|:---:|:---:|:---:|
| $BiVO_4$ | 0 | Yellow |
| Ag/$BiVO_4$ 100 | 0.26 | Khaki |
| Ag/$BiVO_4$ 250 | 0.73 | Dark Green |

From Table 1, we can see that both Ag-containing samples have a wt. % of Ag below 1%. This was desired as, according to the literature, high loadings of Ag NPs on these semiconductors can decrease reactivity of the generated composites in photocatalytic reactions by blocking active sites on the surface of the semiconductor and acting as recombination centres which reduces charge carrier separation efficiency [22,34–36].

The results of this analysis show that, as expected, when the current used during the sputtering process increased from 100 mA to 250 mA, so too did the mass of Ag NPs deposited on the materials. We should then, in turn, be able to measure how these different loadings affect the photocatalytic activity of these materials in the AP reaction.

Ultraviolet-visible diffuse reflectance spectroscopy (UV-Vis DRS) was used to study the light absorption characteristics of these materials and estimate the band gap of $BiVO_4$ before and after sputtering with silver. The spectra are shown in Figure 2.

Each material absorbs strongly in the UV and visible regions of the electromagnetic spectrum. This was expected as the colour of the samples goes from a yellow to a dark green (see Table 1). This agrees with the literature [37]. Pure $BiVO_4$ absorbs the least intensely out of the materials at longer wavelengths. However, upon the incorporation of Ag NPs onto the surface of the materials, the extent of visible light absorption increases greatly in the 800–500 nm (visible) region, with the Ag/$BiVO_4$ 250 sample absorbing more intensely than the 100 mA analogue. The spectra of the sputtered materials show an additional peak at ~600 nm (highlighted in the plot). This is due to the plasmonic absorption by Ag NPs [38]. This SPR band is attributed to longitudinal oscillation of electrons on the NP surface [39], i.e., a surface plasmon.

Tauc plots were used to determine the band gaps of these materials. The results of this analysis are displayed in Table 2. The band gap of $BiVO_4$ was determined to be 2.49 eV. This agrees with related calculations previously shown in the literature [40,41].
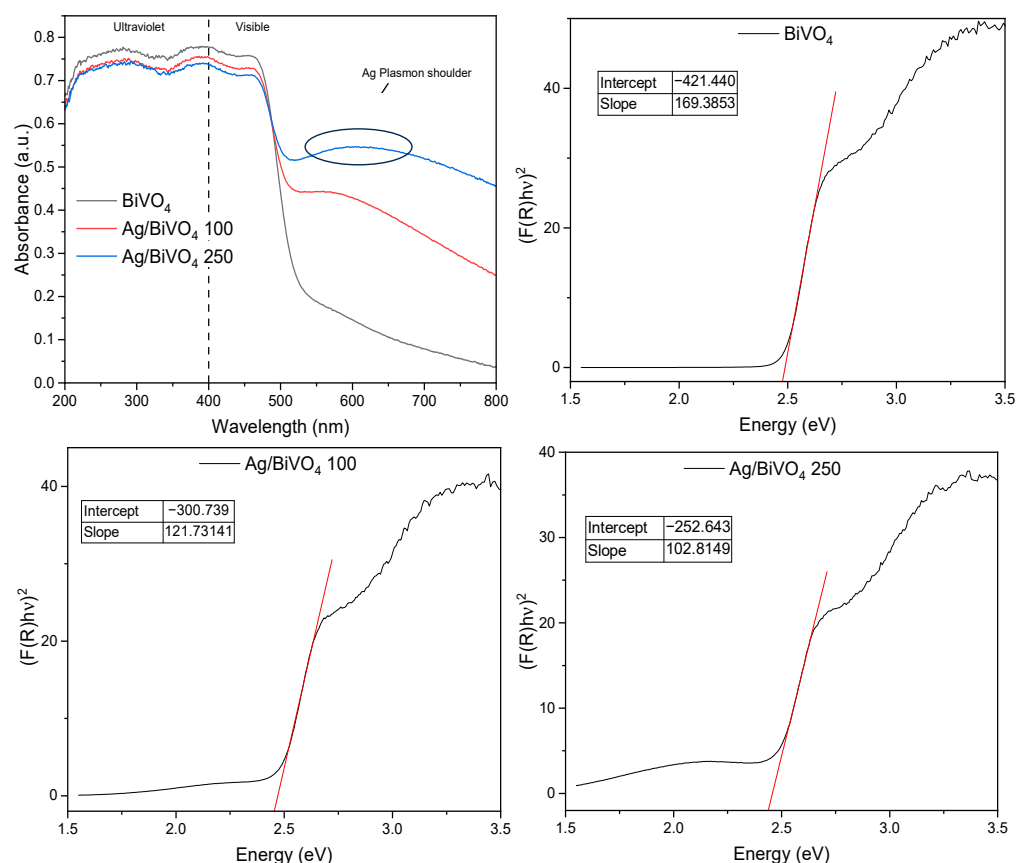
**Figure 2.** UV-Vis DRS spectra of the silver-sputtered $BiVO_4$ materials (**top left**) and their Tauc plots.

**Table 2.** Band gaps of $BiVO_4$ and the Ag-sputtered materials.

| Sample | Band Gap (eV) |
|:---:|:---:|
| $BiVO_4$ | 2.49 |
| $Ag/BiVO_4$ 100 | 2.47 |
| $Ag/BiVO_4$ 250 | 2.46 |

Furthermore, these measurements showed that there is a relatively small apparent decrease in the band gaps of the materials following sputtering of silver onto the surfaces of the semiconductors. The more silver that is deposited on the $BiVO_4$ surface, the greater the apparent reduction in the band gap. Shifting of the VB and CB positions of $BiVO_4$ following doping of Ag into the $BiVO_4$ lattice has been reported where Ag-doping is reported to have moved the positions of both the CB and VB to higher energies (measured using VB-XPS and UV-Vis DRS techniques) [21]. Therefore, this is a possibility that may allow for $BiVO_4$ to (i) absorb more of the visible solar light, and (ii) increase the reduction potentials of the excited electrons in its CB following photon absorption.

Powder X-ray diffraction (XRD) was carried out to confirm the crystalline phases of the materials by comparing their diffraction profiles to reference profiles. The diffractograms of $BiVO_4$, the Ag-sputtered materials, and reference profiles of $Ag^0$ and $BiVO_4$ are displayed in Figure 3.

From Figure 3, we can see that the profile of $BiVO_4$ matches that of the $BiVO_4$ reference profile (JCPDS 83-1698) very well. The sharp peaks indicate high crystallinity of the materials and suggest a large particle size. The $BiVO_4$ materials show several characteristic peaks, for example at 18.9°, 29.1°, and 30.5°, which correspond to reflections from the (011), (121), and (040) planes, respectively [42].
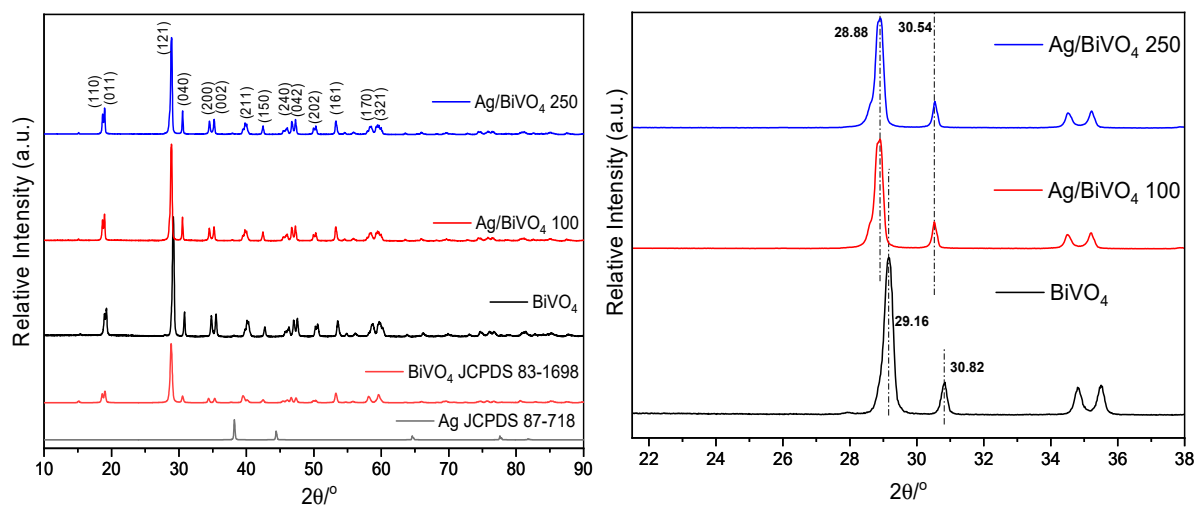
**Figure 3.** XRD profiles of the sputtered $BiVO_4$ materials, and their reference profiles (**left**), and peak shifts between the profiles of unmodified $BiVO_4$ and the Ag-sputtered samples (**right**).

No peaks relating to diffractions from $Ag^0$ were observed in the profiles of the composite. This was to be expected as the loading of Ag on the $BiVO_4$ surfaces is lower than the limit of detection of XRD (~5%). Interestingly, there was a negative shift of 0.28° to lower diffraction angles between the peak maxima in profiles of $BiVO_4$ and the same peaks in the Ag-modified analogues. This suggests that some Ag was substitutionally doped within the $BiVO_4$ lattice. When the dopant atoms are larger in size than those they replace in the lattice ($Ag^0$ has an atomic radius of 144 pm, while $Bi^{3+}$ has an ionic radius of 103 pm [43]), this leads to expansion of the lattice which causes peak shifts to lower angles. This small shift to lower angles of $2\theta$ upon doping of $BiVO_4$ with Ag has been reported in the literature [44]. As Ag is doped within the $BiVO_4$ lattice, this may lead to altering of the band positions which may affect the activity of these materials in the AP reaction.

Transmission electron microscopy (TEM) images of the pure and modified $BiVO_4$ materials were obtained. These were used to gain information on the morphology and sizes of the particles and provide evidence for the existence of Ag NPs on the $BiVO_4$ surfaces. The average particle sizes of $BiVO_4$ and Ag were estimated using ImageJ analysis.

From Figure 4a, we can see that the $BiVO_4$ particles are large and non-uniform in size and shape. The addition of smaller silver particles following magnetron sputtering generates semiconductor:Ag interfaces which may aid reactivity.

In the TEM images of the Ag-sputtered samples (Figure 4b,c), smaller particles were seen on the surface of the larger $BiVO_4$ particles. These were not observed in the TEM images of the unmodified $BiVO_4$ sample and, therefore, are likely Ag particles. The interfaces between the two materials may allow for the transfer of electrons between the two materials, generating heterojunctions and increasing the lifetime of the charge carriers. This should promote reactivity.

Overall, this analysis showed that $BiVO_4$ particles are large (~683 nm) and, following sputtering, smaller Ag particles (23 nm) are seen decorating the surface of $BiVO_4$, leading to the generation of interfaces between the two materials which may promote photocatalysis.

Carbon dioxide temperature programmed desorption ($CO_2$-TPD) profiles are displayed in Figure 5, and the amounts of $CO_2$ desorbed from each material are tabulated in Table 3. Each material showed several desorption events with varying $CO_{2(ads)}$ stabilities and $CO_{2(ads)}$ concentrations. Following deconvolution of the TPD profiles and analysis of the peak areas, it was determined that only 10 µmol of $CO_2$ desorbed per gram of $BiVO_4$. This is likely due to the large particle size and the accompanying low surface area of the

material (see BET, Table 4).  This result agrees with the literature where $CO_2$-TPD from $BiVO_4$ nanosheets showed that $BiVO_4$ adsorbed negligible amounts of $CO_2$ [45].
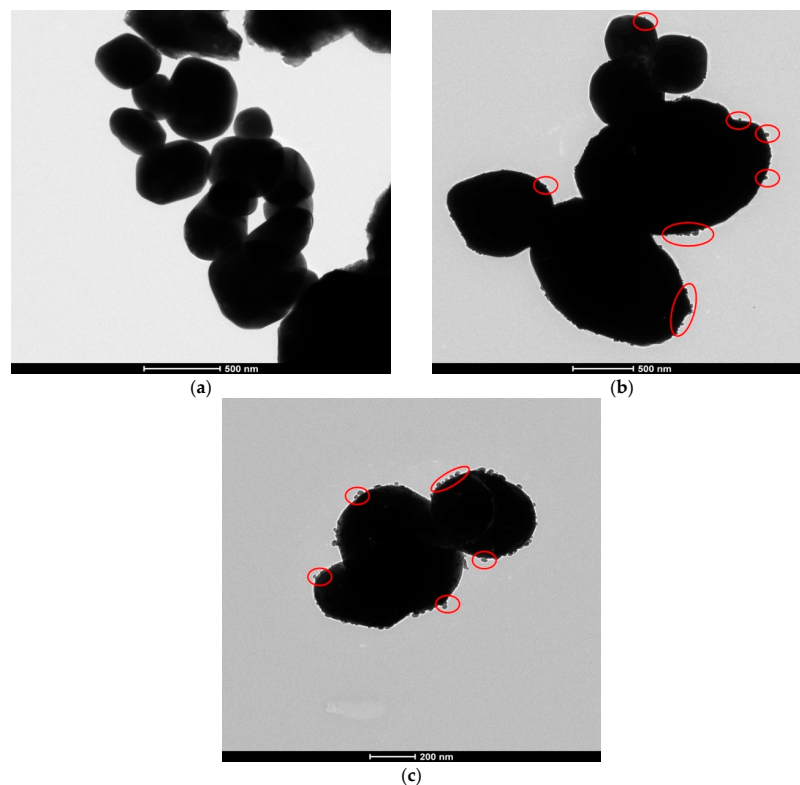


**Figure 4.** TEM micrographs of (**a**) $BiVO_4$, (**b**) $Ag/BiVO_4$ 100, and (**c**) $Ag/BiVO_4$ 250, where the red circles highlight Ag NPs present on $BiVO_4$ surfaces.  Particle size distribution histograms can be found in the Supplementary Material (Figure S1).
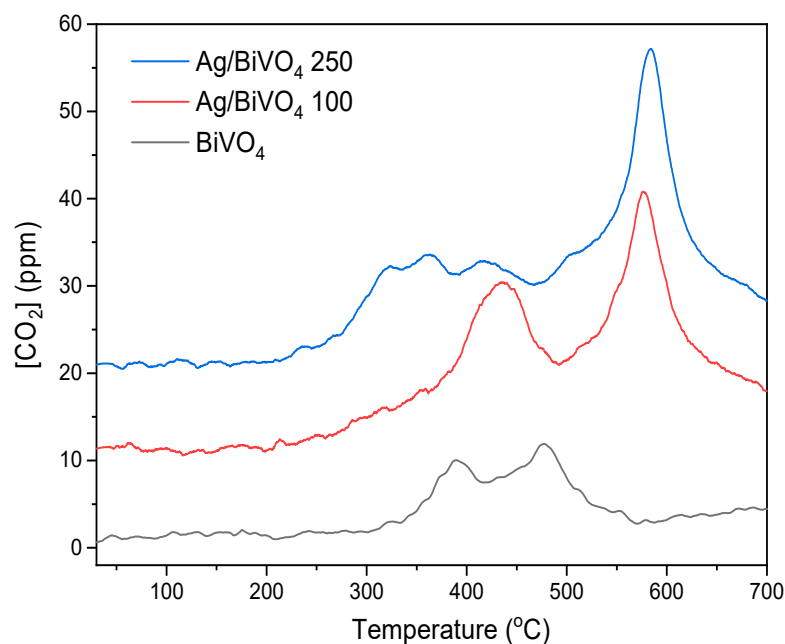


**Figure 5.** $CO_2$-TPD profiles from all three materials.

**Table 3.** Concentrations of desorbed $CO_2$ from each material.

| Sample | [$CO_2$] (µmol/g) | [Ag] (moles/20 mg) |
|---|---|---|
| $BiVO_4$ | 10 | 0 |
| Ag/$BiVO_4$ 100 | 32 | $4.8 \times 10^{-7}$ |
| Ag/$BiVO_4$ 250 | 34 | $1.4 \times 10^{-6}$ |

**Table 4.** BET surface areas of each material.

| Sample | Surface Area ($m^2$/g) |
|---|---|
| $BiVO_4$ | 1.46 |
| Ag/$BiVO_4$ 100 | 1.45 |
| Ag/$BiVO_4$ 250 | 1.45 |

The shape of the TPD profiles from the composite materials differed greatly from the $CO_2$ desorption profile from pure $BiVO_4$, suggesting that the contribution of Ag to the adsorption/desorption process was significant. The addition of Ag led to the development of strong $CO_2$ binding sites. This is evident as the two composite profiles exhibited large desorption peaks centred at approximately 585 °C. This peak was not present in the $CO_2$ desorption profile from $BiVO_4$. The area under this peak increases slightly as the loading of Ag in the composites increases, showing that the adsorption site is either on the Ag particles or at Ag/$BiVO_4$ interfaces. Studies have shown that Ag NPs can adsorb $CO_2$, especially when the Ag has been exposed to oxygen. The O atoms on the surface of Ag can interact with $CO_{2(g)}$ to form carbonate species [46–48]. As these materials were not stored in a protective or inert environment, it is probable that atmospheric oxygen had adsorbed on the surface of the materials, increasing their basicity and, in turn, their ability to adsorb $CO_2$. However, as the proportion of silver on the surface of $BiVO_4$ is low (<1%), the increase in the extents of $CO_2$ adsorption between the samples is not large. Nevertheless, the trend is there.

Furthermore, as the concentration of Ag increases, the $BiVO_4$-derived $CO_2$ adsorption sites (seen at 350–500 °C) became less important and we see desorption from weaker $CO_2$ adsorption sites (peaking at 300–400 °C). This is likely due to the blocking of surface sites on $BiVO_4$ by Ag, but also the generation of new sites at the interfaces. In addition to this, the concentration of $CO_2$ that can be adsorbed increases. Therefore, the addition of Ag leads to the generation of a higher number of weaker $CO_2$ adsorption sites compared to those on pure $BiVO_4$.

From Table 3, we can see that the composites desorb over three times more $CO_2$ than $BiVO_4$. This, along with the increased light absorption of these materials (see Figure 2), should result in higher photocatalytic activity in the AP reaction.

Figure S2 shows the Brunauer–Emmett–Teller (BET) surface area plots collected from the analysis of $BiVO_4$ and the two Ag/$BiVO_4$-sputtered samples. These plots were used to determine the BET surface area of the samples (presented in Table 4).

The surface area of pure $BiVO_4$ was found to be 1.46 $m^2$/g. This low surface area was to be expected when considering the TEM and $CO_2$-TPD results. The surface area of the $BiVO_4$ samples before and after silver sputtering remained unchanged despite the addition of smaller particles to the composite (seen in TEM, Figure 4, and the $CO_2$-TPD analysis, Figure 5).

*3.2. Photocatalytic Activity Measurements*

The photocatalytic activity of these materials in the AP reaction was measured. The results of these experiments are displayed in Figure 6 and the production of $CO_{(g)}$ and

$CH_{4(g)}$ over each material is displayed in Table 5. It should be noted that no products resulted from reactions that were carried out (i) in the dark or (ii) in the absence of catalyst. Additionally, a longer experiment was conducted with Ag/BiVO$_4$ 250, where the material was exposed to irradiation for 72 h. However, this extended exposure did not produce significantly higher levels of reduced $CO_2$ products, indicating that a plateau was reached after 24 h. As a result, subsequent experiments were limited to a maximum duration of 24 h.
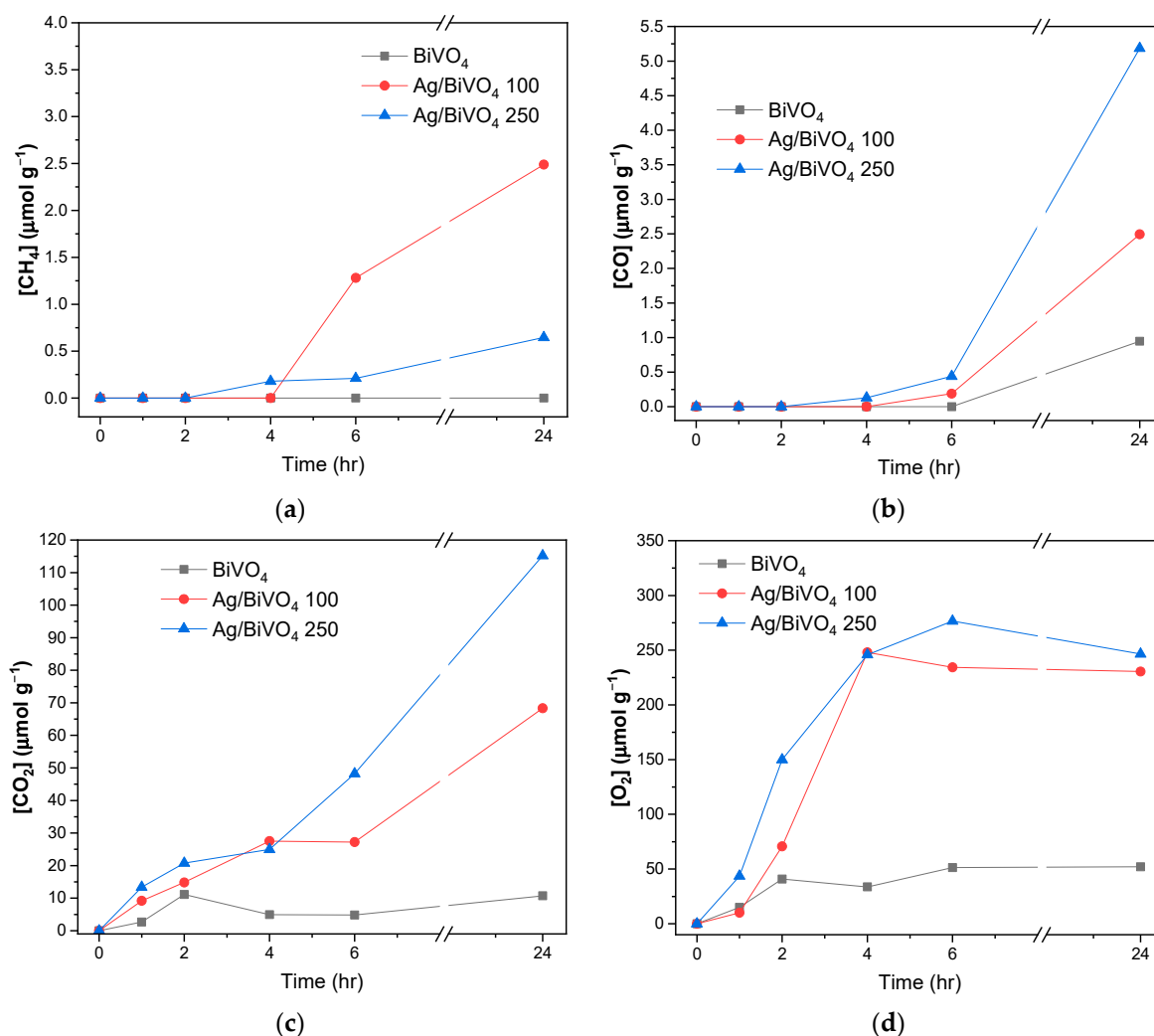


**Figure 6.** Gaseous reactant and product evolution vs. time over the BiVO$_4$ and Ag/BiVO$_4$ catalysts, (**a**) CH$_4$, (**b**) CO, (**c**) CO$_2$, and (**d**) O$_2$.

**Table 5.** Accumulated production of CO and CH$_4$ over each prepared material.

| Sample | CO/$\mu$mol g$^{-1}$ | CH$_4$/$\mu$mol g$^{-1}$ |
|---|---|---|
| BiVO$_4$ | 0.95 | 0 |
| Ag/BiVO$_4$ 100 | 2.49 | 2.49 |
| Ag/BiVO$_4$ 250 | 5.19 | 0.65 |

Since gaseous $CO_2$ is initially present in the reactor at time = 0, the concentration at this point is considered to be 0 $\mu$mol/g. Any subsequent increase in the levels of $CO_2$ in the reactor results from the desorption of $CO_{2(ads)}$ from the catalysts' surfaces, or from the oxidation of reduced hydrocarbonaceous products. Figure 6c) shows the plot of $CO_2$ levels in the reactor over time. The $CO_2$ "evolution" from BiVO$_4$ was very

low, reflecting the results from the TPD analysis where $BiVO_4$ only adsorbed/desorbed approximately 10 $\mu$mol/g. The other two samples show higher levels of $CO_2$ desorption with time, again in line with the TPD results. As we can see in Figure 6d), the $O_2$ levels over time are not consistent with the CO and $CH_4$ evolution levels, i.e., the levels of $O_2$ are not 50% the levels of CO as would be expected from $CO_2$ decomposition reactions ($CO_2 \rightarrow CO + 0.5O_2$). This suggests that perhaps some adsorbed carbon-containing $CO_2$ reduction products also remained adsorbed on the surfaces of the materials and were not detected using GC analysis.

The levels of $O_2$ evolved over the Ag-containing-sputtered composites were much higher than those generated over pure $BiVO_4$. This shows that the modified $BiVO_4$ materials are more active than the unmodified analogue in the AP reaction ($O_2$ being a byproduct of AP). However, the evolution of $O_{2(g)}$ may also reflect decomposition of $Ag_2O$. It has been reported that $Ag_2O$ can decompose into Ag and $O_2$ following absorption of photons [49,50].

The carbon-containing gaseous product that was produced to the greatest extent over the $Ag/BiVO_4$ 250 material was CO. As the level of Ag in the composite increased, so too did the levels of produced CO. This shows that the more "hot" electrons being produced (from excitation of the greater loading of plasmonic Ag), the more $CO_2$ molecules were reduced. CO generation was also observed (albeit to a much lesser extent) over pure $BiVO_4$. Under artificial photosynthesis conditions, $BiVO_4$ has been shown to produce minor amounts of both CO and $CH_3OH$ from $CO_2$ and $H_2O$ [51]. No methanol was observed here; however, Figure S3 shows that $BiVO_4$ post-reaction lost more mass during a TGA experiment compared to the mass lost from a pre-reaction sample, suggesting the presence of combustible surface-adsorbed moieties following reaction, as this extra mass loss occurred between 200 and 300 °C (i.e., the temperature range at which adsorbed hydrocarbonaceous species oxidise/combust).

Possible reasons for the production of CO over pure $BiVO_4$ (despite the fact that the $CB_m$ is not high enough in energy) could be that upon adsorption of $CO_2$, interactions between the semiconductor and the $CO_2$ $\pi$-orbitals lead to a decrease in the reduction activation energy, or perhaps this is merely due to a reaction between $CO_2$ and surface-adsorbed oxygens and hydroxyl groups on $BiVO_4$. Whatever the reason, the level of evolved CO is low, and the conversions carried out over the sputtered materials are higher.

$CH_4$ production was also observed over the composites. This was not noted over unmodified $BiVO_4$. Therefore, we can conclude that the "hot" electrons from Ag play an important role in this reaction, and the mechanism depicted in Figure 7 below may be at play. These hot electrons, combined with the protons produced from water splitting over $BiVO_4$, produce $CH_4$. However, over the material with the higher loading of Ag, the production of $CH_4$ fell. This may be because as less $BiVO_4$ is exposed to reactants (as proportionately more is covered with Ag nanoparticles), there are fewer protons produced and available for this reaction. This agrees with previous reports on the reactivity of $Ag/BiVO_4$ photocatalysts for $CO_2$ reduction using LED light sources [31].

CO was produced in greater quantities than $CH_4$. Thermodynamically, the production of CO is more energy demanding than that of $CH_4$ (see Figure 1). The reduction of one molecule of $CO_2$ may involve as many as eight protons and electrons, the cleavage of C=O bonds, and/or the formation of C-H bonds [52]. Proton-assisted multiple electron transfers are considered more favourable for $CO_2$ reduction reactions [53]. However, CO formation requires only two proton and electron transfers, whereas $CH_4$ formation requires eight (see equations below), which is more challenging from a kinetic point of view [54].
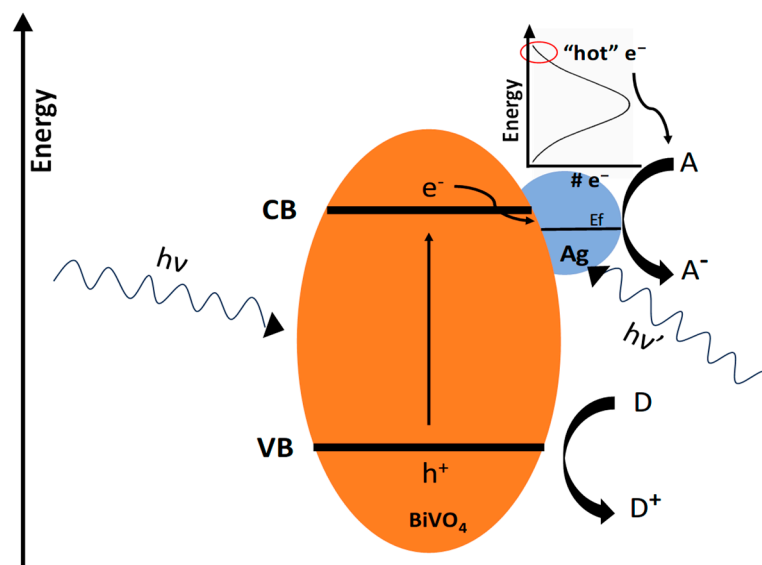
$$CO_{2(g)} + 8H^+ + 8e^- \rightarrow CH_{4(g)} + 2H_2O \tag{1}$$

$$CO_{2(g)} + 2H^+ + 2e^- \rightarrow CO_{(g)} + H_2O \tag{2}$$
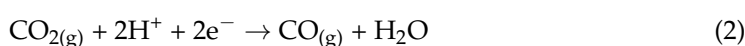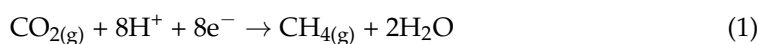
**Figure 7.** Proposed mechanism of a photocatalytic redox reaction over Ag/BiVO$_4$, where "A" is an electron acceptor, "D" is an electron donor, and "VB" and "CB" are valence and conduction bands, respectively.

These reactions are very slow, with the materials requiring approximately 4–6 h of irradiation before any product is observed. Therefore, it is possible that these reactions produce CO as it is kinetically less challenging to produce than CH$_4$. The greater production of CO$_{(g)}$ compared to CH$_{4(g)}$ over Ag/BiVO$_4$ materials is also seen in a study which utilised hydrothermally prepared triangular silver nanoplate-BiVO$_4$ composites for photocatalytic CO$_2$ reduction under LED light sources [31].

Overall, these results show that combining Ag nanoparticles with BiVO$_4$ is beneficial to the reactivity as Ag/BiVO$_4$ 100 and Ag/BiVO$_4$ 250 showed an increase in reactivity for the production of CO$_{(g)}$ and CH$_{4(g)}$ by a factor of 5.2 and 6.3, respectively, compared to the reactivity of pure BiVO$_4$.

*3.3. Post-Reaction Characterisation*

Infrared (IR) analysis was carried out post-reaction on the sputtered samples to determine whether some adsorbed carbon-containing products had been formed over the Ag-containing materials during the reaction. These are displayed below in Figure 8.
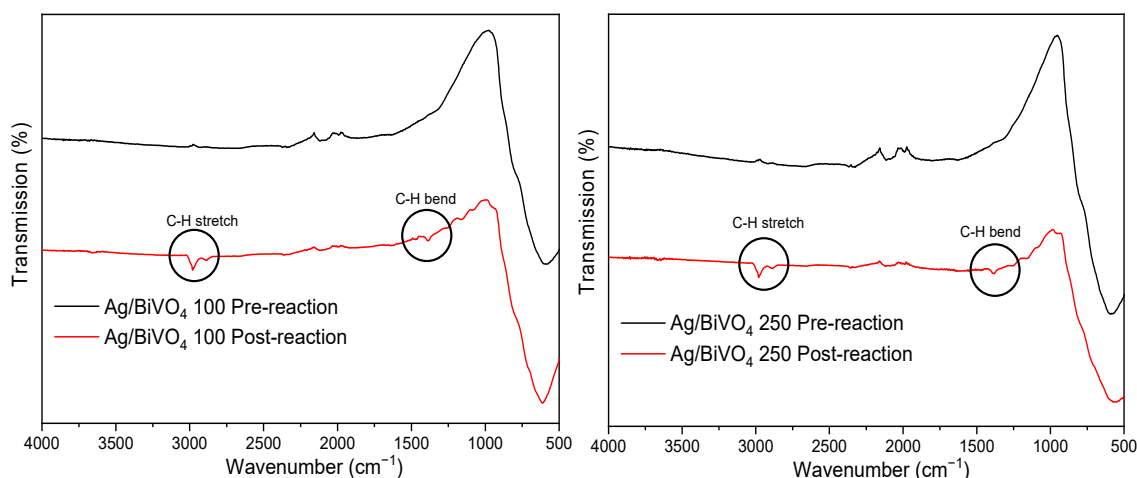


**Figure 8.** Pre- and post-reaction IR spectra of the two Ag-sputtered BiVO$_4$ samples.

The pre-reaction spectra match those seen in the literature [55,56]. Several characteristic peaks can be observed such as those at 475, 600, and 835 cm$^{-1}$, which correspond to the symmetrical stretches of $VO_4^{3-}$, Bi-O-Bi, and V-O, respectively.

The presence of adsorbed hydrocarbonaceous species is confirmed by the post-reaction IR spectra which exhibit peaks relating to C-H vibrations that were not present in the spectrum of the material before the reaction. This includes a peak between 3000 and 2840 cm$^{-1}$, which is due to C-H stretching, and another at 1400 cm$^{-1}$, which corresponds to C-H bending. Additionally, a further peak at 1070 cm$^{-1}$ also appears. The C-O stretch of a primary alcohol typically appears between 1050 and 1080 cm$^{-1}$, suggesting methanol or higher alcohols may have been formed and adsorbed onto the surface of the catalyst during the reaction.

This result suggests that not only did these materials produce gaseous CO and $CH_4$, as detected by GC analysis, but also unidentified adsorbed hydrocarbonaceous materials.

## 4. Conclusions

$BiVO_4$ was prepared using hydrothermal synthesis methods. Ag particles were magnetron sputtered onto the $BiVO_4$ surface at two different Ag loadings. ICP-OES was used to determine the % loading of Ag on the two samples. Powder XRD gave confirmation of the synthesis of $BiVO_4$ and showed that although the loading of Ag was too low to be detected using XRD, there was some evidence of Ag doped into the $BiVO_4$ lattice. UV-Vis spectroscopy was used to calculate the band gaps of the materials and show how the absorption of light increases following incorporation of Ag onto (and into) $BiVO_4$. Furthermore, the presence of the SPR band in the UV-Vis DRS spectra suggests that the Ag is present predominantly in its metallic form (although XPS would be needed to confirm this). $CO_2$-TPD experiments showed that incorporating Ag NPs onto the surface of $BiVO_4$ led to higher levels of desorbed (and, hence, adsorbed) $CO_2$.

Finally, the AP results demonstrated that sputtering $BiVO_4$ with Ag led to an increase in the photocatalytic activity of the materials compared to the reactivity of $BiVO_4$ alone. Both CO and $CH_4$ were produced by the composites, showing a synergistic relationship between the two materials where $BiVO_4$ can split water to provide protons and Ag particles can produce plasmonic "hot" electrons which can be used to reduce $CO_2$. Future experiments to further elucidate the mechanism of reaction would include irradiating with a monochromatic light source with insufficient energy to excite the Ag plasmon in order to confirm the role of "hot" electrons in the AP reaction.

# References

1. Zhang, B.; Sun, L. Artificial photosynthesis: Opportunities and challenges of molecular catalysts. *Chem. Soc. Rev.* **2019**, *48*, 2216–2264. [CrossRef] [PubMed]

2. Wiltshire, A.; Gornall, J.; Booth, B.; Dennis, E.; Falloon, P.; Kay, G.; McNeall, D.; McSweeney, C.; Betts, R. The importance of population, climate change and $CO_2$ plant physiological forcing in determining future global water stress. *Glob. Environ. Chang.* **2013**, *23*, 1083–1097. [CrossRef]

3. Kinney, P.L. Interactions of Climate Change, Air Pollution, and Human Health. *Curr. Environ. Health Rep.* **2018**, *5*, 179–186. [CrossRef] [PubMed]

4. Battin, T.J.; Luyssaert, S.; Kaplan, L.A.; Aufdenkampe, A.K.; Richter, A.; Tranvik, L.J. The boundless carbon cycle. *Nat. Geosci.* **2009**, *2*, 598–600. [CrossRef]

5. Osman, A.I.; Hefny, M.; Abdel Maksoud, M.I.A.; Elgarahy, A.M.; Rooney, D.W. Recent advances in carbon capture storage and utilisation technologies: A review. *Environ. Chem. Lett.* **2021**, *19*, 797–849. [CrossRef]

6. Song, C. $CO_2$ Conversion and Utilization: An Overview. In *$CO_2$ Conversion and Utilization*; ACS: Washington, DC, USA, 2002.

7. Kolobov, N.; Goesten, M.G.; Gascon, J. Metal–Organic Frameworks: Molecules or Semiconductors in Photocatalysis? *Angew. Chem.* **2021**, *60*, 26038–26052. [CrossRef]

8. Yao, S.; He, J.; Gao, F.; Wang, H.; Lin, J.; Bai, Y.; Fang, J.; Zhu, F.; Huang, F.; Wang, M. Highly selective semiconductor photocatalysis for $CO_2$ reduction. *J. Mater. Chem. A Mater. Energy Sustain.* **2023**, *11*, 12539–12558. [CrossRef]

9. Mohan, H.; Vadivel, S.; Rajendran, S. Removal of harmful algae in natural water by semiconductor photocatalysis- A critical review. *Chemosphere* **2022**, *302*, 134827. [CrossRef]

10. Wu, H.; Li, L.; Wang, S.; Zhu, N.; Li, Z.; Zhao, L.; Wang, Y. Recent advances of semiconductor photocatalysis for water pollutant treatment: Mechanisms, materials and applications. *Phys. Chem. Chem. Phys.* **2023**, *25*, 25899–25924. [CrossRef]

11. Wang, F.; Lu, Z.; Guo, H.; Zhang, G.; Li, Y.; Hu, Y.; Jiang, W.; Liu, G. Plasmonic Photocatalysis for $CO_2$ Reduction: Advances, Understanding and Possibilities. *Chem. Eur. J.* **2023**, *29*, 202202716. [CrossRef]

12. Kang, Q.; Ning, S.; Jiang, D.; Wang, Y.; Zhou, F. Semiconductor-based artificial photosynthesis for water-splitting and $CO_2$ reduction. In *Photosynthesis: From Plants to Nanomaterials*; Academic Press: Cambridge, MA, USA, 2023; pp. 377–405.

13. Coronado, J.M.; Fresno, F.; Hernández-Alonso, M.D.; Portela, R. The Role of Co-Catalysts: Interaction and Synergies with Semiconductors. In *Design of Advanced Photocatalytic Materials for Energy and Environmental Applications*; Green Energy and Technology; Springer: London, UK, 2013; Volume 71, pp. 195–216. [CrossRef]

14. Wang, L.; Qi, G.; Liu, X. Ag/$\alpha$-$Fe_2O_3$ nanowire arrays enable effectively photoelectrocatalytic reduction of carbon dioxide to methanol. *J. Power Sources* **2021**, *507*, 230272. [CrossRef]

15. Ueno, K.; Oshikiri, T.; Shi, X.; Zhong, Y.; Misawa, H. Plasmon-induced artificial photosynthesis. *Interface Focus* **2015**, *5*, 20140082. [CrossRef] [PubMed]

16. Tamirat, A.G.; Rick, J.; Dubale, A.A.; Su, W.-N.; Hwang, B.-J. Using hematite for photoelectrochemical water splitting: A review of current progress and challenges. *Nanoscale Horiz.* **2016**, *1*, 243–267. [CrossRef] [PubMed]

17. Min, S.; Wang, F.; Jin, Z.; Xu, J. $Cu_2O$ nanoparticles decorated $BiVO_4$ as an effective visible-light-driven p-n heterojunction photocatalyst for methylene blue degradation. *Superlattices Microstruct.* **2014**, *74*, 294–307. [CrossRef]

18. Ding, K.; Chen, B.; Li, Y.; Zhang, Y.; Chen, Z. Comparative density functional theory study on the electronic and optical properties of $BiMO_4$ (M = V, Nb, Ta). *J. Mater. Chem. A Mater. Energy Sustain.* **2014**, *2*, 8294–8303. [CrossRef]

19. Loka, C.; Gelija, D.; Vattikuti, S.V.P.; Lee, K.-S. Silver-Boosted $WO_3$/$CuWO_4$ Heterojunction Thin Films for Enhanced Photoelectrochemical Water Splitting Efficiency. *ACS Sustain. Chem. Eng.* **2023**, *11*, 11978–11990. [CrossRef]

20. Xu, X.; Du, M.; Chen, T.; Xiong, S.; Wu, T.; Zhao, D.; Fan, Z. New insights into Ag-doped $BiVO_4$ microspheres as visible light photocatalysts. *RSC Adv.* **2016**, *6*, 98788–98796. [CrossRef]

21. Zhu, Z.; Jiang, B.X.; Wu, R.J.; Huang, C.L.; Chang, Y. Photoreduction of $CO_2$ into $CH_4$ Using Novel Composite of Triangular Silver Nanoplates on Graphene-$BiVO_4$. *Catalysts* **2022**, *12*, 750. [CrossRef]

22. Bakhtiarnia, S.; Sheibani, S.; Aubry, E.; Sun, H.; Briois, P.; Arab Pour Yazdi, M. One-step preparation of Ag-incorporated BiVO$_4$ thin films: Plasmon-heterostructure effect in photocatalytic activity enhancement. *Appl. Surf. Sci.* **2022**, *580*, 152253. [CrossRef]

23. Zhang, X.; Chen, Y.L.; Liu, R.-S.; Tsai, D.P. Plasmonic photocatalysis. *Rep. Prog. Phys.* **2013**, *76*, 046401. [CrossRef]

24. Wang, W.; Zhao, Y.; Wang, R. Preparation of Visible-Light-Driven Ag/BiVO$_4$ Photocatalysts and Their Performance for Cr(VI) Reduction. *ChemistrySelect* **2022**, *7*, e202201348. [CrossRef]

25. Sánchez, O.A.; Rodríguez, J.L.; Barrera-Andrade, J.M.; Borja-Urby, R.; Valenzuela, M.A. High performance of Ag/BiVO$_4$ photocatalyst for 2,4-Dichlorophenoxyacetic acid degradation under visible light. *Appl. Catal. A Gen.* **2020**, *600*, 117625. [CrossRef]

26. Mallikarjuna, K.; Vattikuti, S.V.P.; Manne, R.; Manjula, G.; Munirathnam, K.; Mallapur, S.; Marraiki, N.; Mohammed, A.; Reddy, L.V.; Rajesh, M.; et al. Sono-chemical synthesis of silver quantum dots immobilized on exfoliated graphitic carbon nitride nanostructures using ginseng extract for photocatalytic hydrogen evolution, dye degradation, and antimicrobial studies. *Nanomaterials* **2021**, *11*, 2918. [CrossRef] [PubMed]

27. Naughton, E.; Sullivan, J.A. Influence of the presence of RuO$_2$ on the reactivity of Fe$_2$O$_3$ in the artificial photosynthesis reaction. *Sustain. Chem. Environ.* **2024**, *8*, 100167. [CrossRef]

28. Morais, E.; O'Modhrain, C.; Thampi, K.R.; Sullivan, J.A. RuO$_2$/TiO$_2$ photocatalysts prepared via a hydrothermal route: Influence of the presence of TiO$_2$ on the reactivity of RuO$_2$ in the artificial photosynthesis reaction. *J. Catal.* **2021**, *401*, 288–296. [CrossRef]

29. Duan, Z.; Zhao, X.; Wei, C.; Chen, L. Ag-Bi/BiVO$_4$ chain-like hollow microstructures with enhanced photocatalytic activity for CO$_2$ conversion. *App. Catal. A Gen.* **2020**, *594*, 117459. [CrossRef]

30. Xie, Y.-c.; Chen, J.H.; Lin, W.-Y.; Wu, R.-J.; Fegade, U.; Patil, N.; Ansar, S.; Pandey, S. Triangular silver nanoplates-BiVO$_4$ composite for the photocatalytic CO$_2$ reduction under irradiating LED light source. *Opt. Mater.* **2023**, *143*, 114141. [CrossRef]

31. Huang, N.; Li, X.; Xing, T.; Sun, F.; Yang, M.; Yang, J.; Zhao, Y.; Wang, H. Ag Nanoparticle-Decorated BiVO$_4$ Electrodeposited Film as Photoanode for Enhancing the Performance of a Photocatalytic H$_2$O$_2$ Fuel Cell. *Energy Fuels* **2024**, *38*, 19029–19037. [CrossRef]

32. Bai, S.; Li, Q.; Han, N.; Zhang, K.; Tang, P.; Feng, Y.; Luo, R.; Li, D.; Chen, A. Synthesis of novel BiVO$_4$/Cu$_2$O heterojunctions for improving BiVO$_4$ towards NO$_2$ sensing properties. *J. Colloid Interface Sci.* **2020**, *567*, 37–44. [CrossRef]

33. Ge, L.; Han, C.; Liu, J.; Li, Y. Enhanced visible light photocatalytic activity of novel polymeric g-C$_3$N$_4$ loaded with Ag nanoparticles. *Appl. Catal. A Gen.* **2011**, *409–410*, 215–222. [CrossRef]

34. Sun, T.; Jiang, H.Y.; Ma, C.C.; Mao, F.; Xue, B. Ag/g-C$_3$N$_4$ photocatalysts: Microwave-assisted synthesis and enhanced visible-light photocatalytic activity. *Catal. Commun.* **2016**, *79*, 45–48. [CrossRef]

35. Wan, J.; Liu, E.; Fan, J.; Hu, X.; Sun, L.; Tang, C.; Yin, Y.; Li, H.; Hu, Y. In-situ synthesis of plasmonic Ag/Ag$_3$PO$_4$ tetrahedron with exposed {111} facets for high visible-light photocatalytic activity and stability. *Ceram. Int.* **2015**, *41*, 6933–6940. [CrossRef]

36. Booshehri, A.Y.; Chun-Kiat Goh, S.; Hong, J.; Jiang, R.; Xu, R. Effect of depositing silver nanoparticles on BiVO$_4$ in enhancing visible light photocatalytic inactivation of bacteria in water. *J. Mater. Chem. A Mater. Energy Sustain.* **2014**, *2*, 6209–6217. [CrossRef]

37. Huang, K.; Lv, Y.; Zhang, W.; Sun, S.; Yang, B.; Chi, F.; Ran, S.; Liu, X. One-step synthesis of Ag$_3$PO$_4$/Ag photocatalyst with visible-light photocatalytic activity. *Mater. Res.* **2015**, *18*, 939–945. [CrossRef]

38. Singh, S.; Bharti, A.; Meena, V.K. Green synthesis of multi-shaped silver nanoparticles: Optical, morphological and antibacterial properties. *J. Mater. Sci,. Mater. Electron.* **2015**, *26*, 3638–3648. [CrossRef]

39. Fang, W.; Lin, Y.; Xv, R.; Shang, X.; Fu, L. Band-gap and interface engineering by Ni doping and CoPi deposition of BiVO$_4$ photoanode to boost photoelectrochemical water splitting. *Electrochim. Acta* **2023**, *437*, 141511. [CrossRef]

40. Yuan, Y.; Huang, Y.; Ma, F.; Zhang, Z.; Wei, X.; Zhu, G. Structural stability, band structure and optical properties of different BiVO$_4$ phases under pressure. *J. Mater. Sci.* **2016**, *51*, 6662–6673. [CrossRef]

41. Zhong, K.; Gao, H.; Feng, J.; Zhang, Y.; Lai, K. Facile synthesis of Z-scheme Se/BiVO$_4$ heterojunction with enhanced visible-light-driven photocatalytic performance. *J. Mater. Sci.* **2019**, *54*, 10632–10643. [CrossRef]

42. Kelly, A.; Knowles, K.M. *Crystallography and Crystal Defects*, 2nd ed.; John Wiley & Sons: Hoboken, NJ, USA, 2012.

43. Lv, F.Z.; Zhao, W.; Zhong, Y.; Hu, C.H.; Zhou, H.Y.; Chen, R. Synthesis and Photocatalytic Activity of Ag-Doped BiVO$_4$. *Adv. Mater. Res.* **2013**, *734–737*, 2204–2209. [CrossRef]

44. Xu, B.; Zada, A.; Wang, G.; Qu, Y. Boosting the visible-light photoactivities of BiVO$_4$ nanoplates by Eu doping and coupling CeOx nanoparticles for CO$_2$ reduction and organic oxidation. *Sustain. Energy Fuels* **2019**, *3*, 3363–3369. [CrossRef]

45. Barberio, M.; Barone, P.; Imbrogno, A.; Xu, F. CO$_2$ adsorption on silver nanoparticle/carbon nanotube nanocomposites: A study of adsorption characteristics. *Phys. Status Solidi (B) Basic Res.* **2015**, *252*, 1955–1959. [CrossRef]

46. Ye, Y.; Yang, H.; Qian, J.; Su, H.; Lee, K.-J.; Cheng, T.; Xiao, H.; Yano, J.; Goddard, W.A.; Crumlin, E.J.; et al. Dramatic differences in carbon dioxide adsorption and initial steps of reduction between silver and copper. *Nat. Commun.* **2019**, *10*, 1875. [CrossRef] [PubMed]

47. Czanderna, A.W. The interaction of carbon dioxide and ethane with silver. *J. Colloid Interface Sci.* **1966**, *22*, 482–490. [CrossRef]

48. Jiang, L.; Li, Z.; Wang, D.; Guo, T.; Hu, Y. In-situ growth of p-type Ag$_2$O on n-type Bi$_2$O$_2$S with intimate interfacial contact for NIR light-driven photocatalytic CO$_2$ reduction. *Appl. Surf. Sci.* **2022**, *601*, 154185. [CrossRef]

49. Wang, X.; Li, S.; Yu, H.; Yu, J.; Liu, S. Ag$_2$O as a New Visible-Light Photocatalyst: Self-Stability and High Photocatalytic Activity. *Chem. Eur. J.* **2011**, *17*, 7777–7780. [CrossRef]

50. Wang, X.; Wang, Y.; Gao, M.; Shen, J.; Pu, X.; Zhang, Z.; Lin, H.; Wang, X. BiVO$_4$/Bi$_4$Ti$_3$O$_{12}$ heterojunction enabling efficient photocatalytic reduction of CO$_2$ with H$_2$O to CH$_3$OH and CO. *Appl. Catal. B Environ.* **2020**, *270*, 118876. [CrossRef]

51. Chang, X.; Wang, T.; Gong, J. CO$_2$ photo-reduction: Insights into CO$_2$ activation and reaction on surfaces of photocatalysts. *Energy Environ. Sci.* **2016**, *9*, 2177–2196. [CrossRef]

52. Hiragond, C.; Ali, S.; Sorcar, S.; In, S.-I. Hierarchical Nanostructured Photocatalysts for CO$_2$ Photoreduction. *Catalysts* **2019**, *9*, 370. [CrossRef]

53. Wu, H.; Kong, X.Y.; Wen, X.; Chai, S.P.; Lovell, E.C.; Tang, J.; Ng, Y.H. Metal–Organic Framework Decorated Cuprous Oxide Nanowires for Long-lived Charges Applied in Selective Photocatalytic CO$_2$ Reduction to CH$_4$. *Angew. Chem. (Int. Ed.)* **2021**, *60*, 8455–8459. [CrossRef]

54. Yang, R.; Zhu, R.; Fan, Y.; Hu, L.; Chen, Q. In situ synthesis of C-doped BiVO$_4$ with natural leaf as a template under different calcination temperatures. *RSC Adv.* **2019**, *9*, 14004–14010. [CrossRef]

55. Regmi, C.; Dhakal, D.; Lee, S.W. Visible-light-induced Ag/BiVO$_4$ semiconductor with enhanced photocatalytic and antibacterial performance. *Nanotechnology* **2018**, *29*, 064001. [CrossRef] [PubMed]

56. Li, Y.; Duan, X.; Qian, Y.; Yang, L.; Liao, H. Nanocrystalline Silver Particles: Synthesis, Agglomeration, and Sputtering Induced by Electron Beam. *J. Colloid Interface Sci.* **1999**, *209*, 347–349. [CrossRef] [PubMed]